



Universality of local weak interactions and its application for interferometric alignment

Jan Dziewior^{a,b}, Lukas Knips^{a,b}, Demitry Farfurnik^{c,1}, Katharina Senkalla^{a,b}, Nimrod Benschalom^c, Jonathan Efroni^c, Jasmin Meinecke^{a,b}, Shimshon Bar-Ad^c, Harald Weinfurter^{a,b}, and Lev Vaidman^{c,2}

^aMax-Planck-Institut für Quantenoptik, 85748 Garching, Germany; ^bDepartment für Physik, Ludwig-Maximilians-Universität, 80797 München, Germany; and ^cRaymond and Beverly Sackler School of Physics and Astronomy, Tel-Aviv University, Tel-Aviv 69978, Israel

Edited by Michael Berry, University of Bristol, Bristol, UK, and approved December 31, 2018 (received for review July 28, 2018)

The modification of the effect of interactions of a particle as a function of its preselected and postselected states is analyzed theoretically and experimentally. The universality property of this modification in the case of local interactions of a spatially preselected and postselected particle has been found. It allowed us to define an operational approach for the characterization of the presence of a quantum particle in a particular place: the way it modifies the effect of local interactions. The experiment demonstrating this universality property provides an efficient interferometric alignment method, in which the position of the beam on a single detector throughout one phase scan yields all misalignment parameters.

quantum physics | quantum experiments | quantum measurement | weak measurements | optics alignment

Preselected and postselected systems are ubiquitous in quantum mechanics. In many quantum information schemes, the intended process is only realized by the interplay of preselection and postselection. The addition of postselection, often together with conditioned transformations, is the basis of protocols such as universal quantum computation within the Knill–Laflamme–Milburn scheme (1), entanglement swapping (2), and heralding in general (3).

The two-state vector formalism (TSVF) (4) provides a general framework for the description of preselected and postselected systems. It introduces a state evolving backward in time and thereby treats the postselection on equal footing as the preselection. The key element of the TSVF is the weak value of an observable. As long as the interaction is sufficiently weak or short, the observable effect on the external system is completely characterized by the weak value (5). For such interactions, the state of the external systems after the postselection can deviate significantly from the states expected by just considering the coupling to preselected systems (6). The concept of weak values became the basis of several successful applications in precision-measurement techniques (7, 8). While there are theoretical controversies about the optimality of the weak value-based tomography and precision-measurement methods (9–20), a plethora of fruitful applications continues to emerge (21–34).

We take a step back and investigate the fundamental properties of preselected and postselected systems. We find that there exists a general universality principle characterizing how the effects of the interactions in one location of a spatially preselected and postselected quantum system are modified as a function of preselection and postselection. All these modifications are specified by a single complex number, the weak value of the spatial projection operator. One of the innovations of our approach is that it does not rely on the specific form of the interaction Hamiltonian. Instead, it expresses the change of the state via the complex amplitude of an orthogonal component, which emerges due to the interaction. If the weak value is a positive number, the size of the changes in every variable is multiplied by this number, and when it is negative, all modifications happen in

the opposite direction. If the effect originally changed a particular variable, in the case of an imaginary weak value, the effect will occur in a variable conjugate to the initial one, and when the weak value is a complex number, both effects are combined together. This approach allows a formal definition of a quantum particle's presence.

Until now, most accounts considered the weak value to be limited to the case of weak interactions—e.g., refs. 35–39. It is another crucial innovation of our approach, however, that we explicitly apply the formalism to the case of much stronger interactions. We use an expression for the weak value which takes into account changes due to interactions of finite strength in the time interval between preselection and postselection. Besides incorporating the stronger interactions, we also account for decoherence or imperfections in the measurement system. We show experimentally that this weak value can in fact be measured by using weakly coupled pointers.

An interferometer, especially a Mach–Zehnder-type interferometer (MZI), can be seen as the iconic example for preselected and postselected systems. The reflectivity/transmittivity of the first beam splitter together with the phase shifter defines the preselected state of the system. The final beam splitter together

Significance

In this combined theoretical and experimental work, we describe and demonstrate a universal feature of local couplings of spatially preselected and postselected systems. All weak couplings, independently of their physical nature, are modified in the same universal manner, characterized by the weak value of local projection. We present a general analysis which neither relies on a specific form of the coupling nor is restricted to weak interactions. This allows us to define a consistent paradigm of the presence of a quantum particle, much more intricate than the concept of the presence of a classical particle. Furthermore, we discovered that Gaussian pointers remain reliable beyond the weak regime, which enabled a simple and efficient alignment method for interferometric setups.

Author contributions: J.D., L.K., H.W., and L.V. designed research; J.D., L.K., K.S., and L.V. performed research; J.D., L.K., D.F., and L.V. contributed new analytic tools; J.D., L.K., D.F., K.S., N.B., J.E., S.B.-A., and L.V. analyzed data; J.D., L.K., K.S., N.B., J.M., H.W., and L.V. wrote the paper; D.F., N.B., J.E., and S.B.-A. performed preliminary experimental work on the alignment method; D.F., N.B., J.E., and S.B.-A. participated in the analyses; and D.F. suggested the alignment method.

The authors declare no conflict of interest.

This article is a PNAS Direct Submission.

This open access article is distributed under [Creative Commons Attribution License 4.0 \(CC BY\)](https://creativecommons.org/licenses/by/4.0/).

Data deposition: Please contact the authors if you wish to access the raw data.

¹Present addresses: Racah Institute of Physics, The Hebrew University of Jerusalem, Jerusalem 9190401, Israel; and The Center for Nanoscience and Nanotechnology, The Hebrew University of Jerusalem, Jerusalem 9190401, Israel.

²To whom correspondence should be addressed. Email: vaidman@post.tau.ac.il.

Published online February 5, 2019.

For the particle that has passed through the corresponding MZI and has been detected in C , we observe a different change of the state of the external systems. Expanding Eq. 6 in orders of ϵ , we can see that the weak effect of the interaction is modified relative to [7] by a single parameter, the weak value of projection on arm A ,

$$|\chi\rangle \rightarrow |\tilde{\chi}\rangle = |\chi\rangle + \epsilon (\mathbf{P}_A)_w |\chi^\perp\rangle + \mathcal{O}(\epsilon^2), \quad [8]$$

where, for defining the weak value, we neglect the coupling to external systems

$$(\mathbf{P}_A)_w \equiv \frac{\langle \phi | \mathbf{P}_A | \psi \rangle}{\langle \phi | \psi \rangle} = \frac{1}{1 + \tan \alpha e^{i\varphi}}. \quad [9]$$

The design of the interferometer allows the full range of weak values of projection onto arm A , by varying the parameters $\tan \alpha$ and φ . Note that we did not restrict the number of interactions as long as their combined effect is sufficiently weak.

When the trace left in the interferometer is small, $\epsilon \ll 1$, the weak value can be considered neglecting the effect of the interactions, as in [9]. In the next section, we will turn toward scenarios with stronger couplings for which the interactions cannot be neglected.

Weak Value Considering Finite Coupling Strength and Imperfections

Calculating the weak value as in Eq. 9, we have implicitly assumed that it only depends on the preselection and postselection states at the boundaries of the considered time interval. This is correct in the limit of weak coupling, which is considered in most works about weak measurements. However, sometimes even in scenarios with coupling of finite strength, the weak value has been treated as if there was no coupling—i.e., using formula [9] (20, 35–40).

To correctly account for couplings of finite strength, we turn to the proper definition of the weak value in the framework of the TSVF, which refers to a single point in time t , at which the particular forward- and backward-evolving quantum states have to be evaluated (41). All interactions of finite strength and imperfections of optical devices between preselection and t , as well as between t and postselection, must be considered. Thus, Eq. 2 correctly describes the forward-evolving state only immediately after the first beam splitter, and Eq. 4 describes the backward-evolving state only immediately before the second beam splitter. Since all evolutions due to imperfections or interactions with the different external systems are local—i.e., they have the common eigenstates $|A\rangle$ and $|B\rangle$ —the time ordering of the evolutions is of no consequence. Therefore, the weak value $(\mathbf{P}_A)_w$ stays constant in time, and we are free to choose any moment in time to calculate it. For convenience, we calculate the weak value immediately before postselection on state [4] and modify only the forward-evolving state to account for the evolution due to interactions inside the interferometer.

Due to the interactions, the system becomes entangled with the external systems as described by Eq. 5. Thus, the particle is in the mixed state described by the density matrix in the basis $\{|A\rangle, |B\rangle\}$

$$\rho = \begin{pmatrix} \cos^2 \alpha & \cos \alpha \sin \alpha e^{-i\varphi} \eta \\ \cos \alpha \sin \alpha e^{i\varphi} \eta & \sin^2 \alpha \end{pmatrix}. \quad [10]$$

The weak value in the case of mixed states has been derived in ref. 5 (equation 32 therein),

$$A_w = \frac{\text{Tr}(\rho_{\text{post}} A \rho_{\text{pre}})}{\text{Tr}(\rho_{\text{post}} \rho_{\text{pre}})}. \quad [11]$$

In our case, this formula is not applicable for arbitrary time between the preselection and postselection due to entanglement in both forward- and backward-evolving states with the same external systems (section VI of ref. 5), but it can be used to calculate the weak value immediately before the last beam splitter since the backward-evolving state is not entangled (see also refs. 35, 42, and 43). As we explained above, the weak value of the projector \mathbf{P}_A is constant between preselection and postselection, so it can be calculated as

$$(\mathbf{P}_A)_w = \frac{\text{Tr}(|\phi\rangle\langle\phi| \mathbf{P}_A \rho)}{\text{Tr}(|\phi\rangle\langle\phi| \rho)} = \frac{1 + \tan \alpha \eta e^{-i\varphi}}{1 + \tan^2 \alpha + 2 \tan \alpha \eta \cos \varphi}. \quad [12]$$

From Eq. 10, we see that the overlap η quantifies the loss of coherence between the two arms of the interferometer due to interactions and imperfections, which consequently leads to a reduction of the maximally achievable weak value. The dependence of the weak value [12] on η as well as on α and φ is presented in Fig. 2. Fig. 2 A and B show the case with ideal overlap $\eta=1$, while Fig. 2 C – F illustrate the dependence for the nonideal case with reduced overlap and thus smaller $(\mathbf{P}_A)_w$.

The weak value [12] which accounts for multiple and even strong interactions is not useful to describe the whole of the external systems when inserted into expansion [8] because ϵ is large. However, Eq. 12 can be used to describe the modification for those interactions which are weak, even if some of the other interactions or all of them together are arbitrarily strong. We will show this now.

In our scenario, we neglect the interactions of external systems in arm A among themselves. If between some particular systems, the interaction cannot be neglected, they are considered as a single composite system. Thus, the interactions [1] in a single channel (Fig. 1A) can be decomposed as

$$|\chi\rangle = \bigotimes_j |\chi_j\rangle \rightarrow |\chi'\rangle = \bigotimes_j \eta_j (|\chi_j\rangle + \epsilon_j |\chi_j^\perp\rangle). \quad [13]$$

Here, as for [1], we absorbed the phases in the definitions of states, such that ϵ_j and η_j are positive numbers.

In the case where the coupling to the, say, k -th system, is weak, the change of the state of the system can be also expressed by using density-matrix language in the $\{|\chi_k\rangle, |\chi_k^\perp\rangle\}$ basis as

$$\rho_k = \begin{pmatrix} 1 & 0 \\ 0 & 0 \end{pmatrix} \rightarrow \rho'_k = \begin{pmatrix} 1 & \epsilon_k \\ \epsilon_k & 0 \end{pmatrix} + \mathcal{O}(\epsilon_k^2). \quad [14]$$

For a particle passing through the MZI, when both the preselection as well as the postselection state are superpositions of $|A\rangle$ and $|B\rangle$, several interactions in A (Fig. 1B) will lead to entanglement between the various external systems. Thus, each of the systems will be described by a mixed state. The modified evolution of the weakly coupled k -th system is

$$\rho_k \rightarrow \tilde{\rho}_k = \begin{pmatrix} 1 & (\mathbf{P}_A)_w^* \epsilon_k \\ (\mathbf{P}_A)_w \epsilon_k & 0 \end{pmatrix} + \mathcal{O}(\epsilon_k^2). \quad [15]$$

Again, the modification of the effect of the weak interaction is characterized by the weak value $(\mathbf{P}_A)_w$.

Manifestation of the Trace as Shifts in Pointer States

In the previous sections, we described the trace a particle leaves as the appearance of an orthogonal component in the quantum state of external systems. Another language, frequently closer to

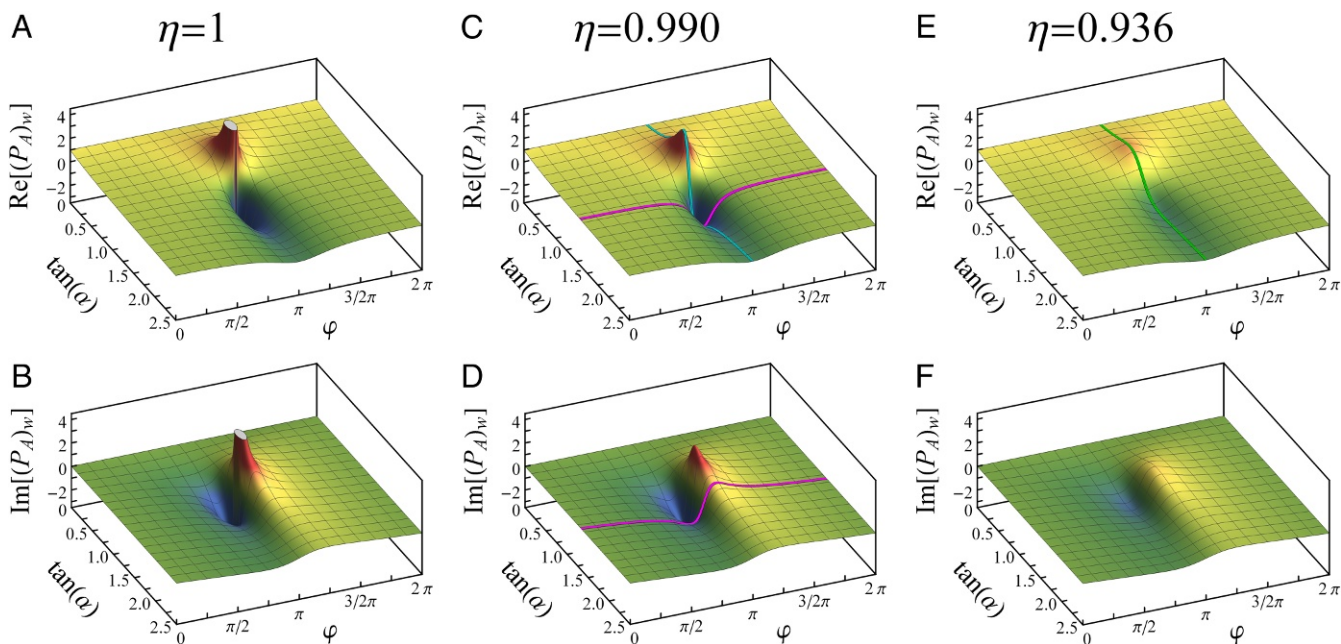


Fig. 2. Exact parameter dependence of weak value. Real (A, C, and E) and imaginary (B, D, and F) parts of weak value of the projection operator on arm A for $\eta = 1$, $\eta = 0.990$, and $\eta = 0.936$. Each plot shows the dependence on the phase φ and the amplitude ratio $\tan \alpha$. The highlighted colored lines represent the parameter values that are set in the various measurements (see Figs. 4 and 5).

experimental evidence, is the change in the expectation values of the external systems. Given the small change due to interactions in Fig. 1A, expressed in [7], every observable O of the external system changes its expectation value as

$$\delta \langle O \rangle \equiv \langle \chi' | O | \chi' \rangle - \langle \chi | O | \chi \rangle = 2\epsilon \operatorname{Re} \left[\langle \chi | O | \chi^\perp \rangle \right] + \mathcal{O}(\epsilon^2). \quad [16]$$

Then, using [8] (or [15], respectively), we see that for the preselected and postselected particle (Fig. 1B), the change in the expectation value of O is modified according to

$$\tilde{\delta} \langle O \rangle = 2\epsilon \operatorname{Re} \left[\langle \chi | O | \chi^\perp \rangle (\mathbf{P}_A)_w \right] + \mathcal{O}(\epsilon^2). \quad [17]$$

This formula is universal—it is valid for every system which was coupled weakly in arm A to the particle passing through the interferometer.

Eq. 17 represents a result in a very general scenario. Let us now focus on the less general but very common measurement situation, which is usually considered when treating weak values (41). There, a single observable O is the pointer variable Q , the pointer wavefunction $\chi(Q)$ is real, and the interaction with the particle in the channel shifts the wave function in the pointer variable representation as

$$\chi(Q) \rightarrow \chi'(Q) = \chi(Q - \delta Q). \quad [18]$$

Obviously, this also shifts the expectation value

$$\delta \langle Q \rangle = \delta Q. \quad [19]$$

In this scenario, $\chi^\perp(Q)$ is also real, as well as $\langle \chi | Q | \chi^\perp \rangle$. Then, a positive weak value $(\mathbf{P}_A)_w$ just tells us how the effect of the interaction is amplified or reduced according to

$$\tilde{\delta} \langle Q \rangle \approx \delta Q \operatorname{Re}[(\mathbf{P}_A)_w]. \quad [20]$$

If $(\mathbf{P}_A)_w$ is negative, it tells us that the pointer will be shifted in the opposite direction.

If the weak value is imaginary, the expectation value of the pointer position will not be changed. However, an orthogonal component in the quantum state of the pointer will still appear. It will manifest itself in the shift of the expectation value of the momentum P_Q conjugate to Q

$$\tilde{\delta} \langle P_Q \rangle \approx 2\delta Q (\Delta P_Q)^2 \operatorname{Im}[(\mathbf{P}_A)_w], \quad [21]$$

where $(\Delta P_Q)^2 = \langle \chi | P_Q^2 | \chi \rangle - \langle \chi | P_Q | \chi \rangle^2$ and $\hbar = 1$.

Eqs. 20 and 21 were obtained from [16] and [17] on the assumption of weak coupling when higher orders of ϵ can be neglected. In the measurement situation [18] with a Gaussian pointer, $\chi = e^{-Q^2/4(\Delta Q)^2}$ (we omit normalization), the usual range of validity of the weak value formalism is extended. Even when the coupling is strong and the pointer distribution is significantly distorted during the measurement, the expressions for the shifts of the expectation values of Q , [16] and [17], remain exact, with

$$\delta \langle Q \rangle = 2\epsilon \operatorname{Re} \left[\langle \chi | Q | \chi^\perp \rangle \right], \quad [22a]$$

$$\tilde{\delta} \langle Q \rangle = 2\epsilon \operatorname{Re} \left[\langle \chi | Q | \chi^\perp \rangle (\mathbf{P}_A)_w \right]. \quad [22b]$$

Indeed, for the Gaussian pointer $\langle \chi | Q | \chi \rangle = 0$, $\langle \chi' | Q | \chi' \rangle = \delta Q$, and also the following expressions are easily calculated as

$$\eta = \langle \chi | \chi' \rangle = e^{-(\delta Q)^2/8(\Delta Q)^2}, \quad \langle \chi | Q | \chi' \rangle = \langle \chi | \chi' \rangle \frac{\delta Q}{2}. \quad [23]$$

Then, [22a] is proven by substituting [19] and [1], while including [6] and [12] proves [22b].

If the pointer is a Gaussian in the position variable Q , it is of course also a Gaussian in the conjugate momentum P_Q representation. Therefore, [20] and [21], in analogy to the above, become exact formulas with $\Delta P_Q = \frac{1}{2\Delta Q}$. There are corresponding exact formulas for the effect of a shift in momentum δP_Q with

$$\tilde{\delta}\langle P_Q \rangle = \delta P_Q \text{Re}[(\mathbf{P}_A)_w], \quad [24a]$$

$$\tilde{\delta}\langle Q \rangle = -2\delta P_Q (\Delta Q)^2 \text{Im}[(\mathbf{P}_A)_w], \quad [24b]$$

see also ref. 44.

Direct substitution shows that the expressions remain correct for Gaussians in the regime of strong interactions also in the case of combinations of shifts in Q and P_Q , such that

$$\tilde{\delta}\langle Q \rangle = \delta Q \text{Re}[(\mathbf{P}_A)_w] - 2\delta P_Q (\Delta Q)^2 \text{Im}[(\mathbf{P}_A)_w], \quad [25a]$$

$$\tilde{\delta}\langle P_Q \rangle = \delta P_Q \text{Re}[(\mathbf{P}_A)_w] + \frac{\delta Q}{2(\Delta Q)^2} \text{Im}[(\mathbf{P}_A)_w]. \quad [25b]$$

These equations are the basis of the alignment method presented in Alignment Method.

Observing the Universality Property

We use an optical MZI to experimentally visualize our central claim—namely, that all kinds of small effects of spatially preselected and postselected systems taking place at a specific location are modified in a universal manner characterized by the weak value of spatial projection. In the experiment, we demonstrate the universal change for three different couplings. In every case, the effect is modified in the same manner.

There are proposals and actual experiments where the photon couples to other particles in one arm of the interferometer (45–49). In ref. 49, one arm of the interferometer is a Kerr medium, and the photon passing through this arm changes the quantum state of the pointer by introducing a shift in the relative phase between the wave packets of the pointer photons. As it is done in most weak-measurement experiments, instead of coupling to external particles, we, rather, study interactions of the photons in an arm of the interferometer by observing the effect on other degrees of freedom of the photons itself. We also used a (weak) laser beam, so all of the results can be explained by using Maxwell equations (although in a much more difficult way), but the observations would not change by using single photons, since intensity measurements are in one-to-one correspondence to single-photon probability distributions.

The interactions in arm A are realized by introducing controlled changes of spatial and polarization degrees of freedom. The initial state of the position degree of freedom can be well approximated by a Gaussian along the x as well as the y coordinates. The interaction is implemented by shifting the center of the Gaussian intensity distribution of the light beam going through arm A by δx , compared with the beam going through arm B ,

$$\chi_x(x) = e^{-x^2/w_0^2} \rightarrow \chi'_x(x) = e^{-(x-\delta x)^2/w_0^2}, \quad [26]$$

where w_0 denotes the waist of the beam and normalization factors are omitted.

Another degree of freedom is the spatial state in the y direction of the light beam, which we modified by changing the angle of the beam around the x axis, which for small angles corresponds to the momentum shift $\delta p_y = \frac{2\pi}{\lambda} \delta \theta_x$. The resulting modification in arm A can be expressed by

$$\chi_y(p_y) = e^{-w_0^2 p_y^2/4} \rightarrow \chi'_y(p_y) = e^{-w_0^2 (p_y - \delta p_y)^2/4}. \quad [27]$$

As a third external system, we use the photon polarization. The interaction parameter here is the rotation of polarization by the angle $\delta\Theta$,

$$|\chi_\sigma\rangle = |H\rangle \rightarrow |\chi'_\sigma\rangle = \cos \frac{\delta\Theta}{2} |H\rangle + \sin \frac{\delta\Theta}{2} |V\rangle, \quad [28]$$

where the states $|H\rangle$ and $|V\rangle$ are defined via $\sigma_z |H\rangle = |H\rangle$ and $\sigma_z |V\rangle = -|V\rangle$ for the Pauli matrix σ_z .

All other properties of the photon are expressed in the state $|\chi_O\rangle$. Any imperfections of the interferometer can be understood to lead to a change of the initial state of these properties in arm A , $|\chi_O\rangle \rightarrow |\chi'_O\rangle$.

It is a good approximation to assume that there are no interactions between the external degrees of freedom we consider, and thus we can express the quantum state of the photon in arm B just before reaching the final beam splitter of the interferometer as

$$|B\rangle|\chi\rangle = |B\rangle|\chi_x\rangle|\chi_y\rangle|\chi_\sigma\rangle|\chi_O\rangle, \quad [29]$$

while in arm A it is

$$|A\rangle|\chi'\rangle = |A\rangle|\chi'_x\rangle|\chi'_y\rangle|\chi'_\sigma\rangle|\chi'_O\rangle. \quad [30]$$

To test the universality of modifications of effects for various degrees of freedom, one could either perform complete tomographies of the final pointer states [14] and [15] or, more clearly, show the modification of the effects of the three couplings according to [20] and [21]. We follow the second approach. More explicitly, we test the differences between effects of the interactions on the expectation values in three degrees of freedom when the particle passes through the single arm (expressed by δ) and when the particle passes through both arms (expressed by $\tilde{\delta}$).[‡] Because of the linear relation between θ_y and p_x , as well as θ_x and p_y , one obtains

$$\tilde{\delta}\langle x \rangle = \delta\langle x \rangle \text{Re}[(\mathbf{P}_A)_w], \quad [31]$$

$$\tilde{\delta}\langle \theta_y \rangle = \frac{\delta\langle x \rangle}{z_R} \text{Im}[(\mathbf{P}_A)_w], \quad [32]$$

$$\tilde{\delta}\langle \theta_x \rangle = \delta\langle \theta_x \rangle \text{Re}[(\mathbf{P}_A)_w], \quad [33]$$

$$\tilde{\delta}\langle y \rangle = -z_R \delta\langle \theta_x \rangle \text{Im}[(\mathbf{P}_A)_w]. \quad [34]$$

Here, we have used the Rayleigh range $z_R \equiv \frac{\pi w_0^2}{\lambda}$ as the characteristic parameter of the Gaussian beam.

The conjugate variable to the angle Θ defining polarization changes in the $\sigma_x - \sigma_z$ plane is an angle Υ describing polarization rotations in the $\sigma_y - \sigma_z$ plane relative to the initial state $|H\rangle$. For small deviations, these angles relate linearly to $\langle \sigma_x \rangle$ and $\langle \sigma_y \rangle$, respectively, and are given by

$$\tilde{\delta}\langle \Theta \rangle = \delta\langle \Theta \rangle \text{Re}[(\mathbf{P}_A)_w], \quad [35]$$

$$\tilde{\delta}\langle \Upsilon \rangle = -\delta\langle \Theta \rangle \text{Im}[(\mathbf{P}_A)_w]. \quad [36]$$

The test was performed for the full range of φ and thus for a large range of values $(\mathbf{P}_A)_w$; see violet lines on the graphs of Fig. 2. The parameters for the calculation of $(\mathbf{P}_A)_w$ necessary for testing relations [31–36] were also obtained from measurements. The signals from separate arms (when the other arm was blocked) provided $\tan \alpha$. The phase φ and the overlap η were obtained from the intensity of the interference signal and visibility measurements, respectively. The relation between the visibility \mathcal{V} and the overlap η for the phase-dependent output intensity $\mathcal{I} \propto \langle \phi | \rho | \phi \rangle \propto 1 + \tan^2 \alpha + 2 \tan \alpha \eta \cos \varphi$ is given by

$$\mathcal{V} \equiv \frac{\mathcal{I}_{\max} - \mathcal{I}_{\min}}{\mathcal{I}_{\max} + \mathcal{I}_{\min}} = \eta \frac{2 \tan \alpha}{1 + \tan^2 \alpha}. \quad [37]$$

The experiment is shown schematically in Fig. 3. After propagation through a single-mode fiber for spatial filtering, the horizontally polarized light from a laser diode ($\lambda = 780$ nm) is split by

[‡]We chose this method since our measurements of the shifts $\delta\langle x \rangle$, $\delta\langle \theta_x \rangle$, and $\delta\langle \Theta \rangle$ in a single channel are more precise than our control of the shifts δx , $\delta \theta_x$, and $\delta \Theta$ via manual stages.

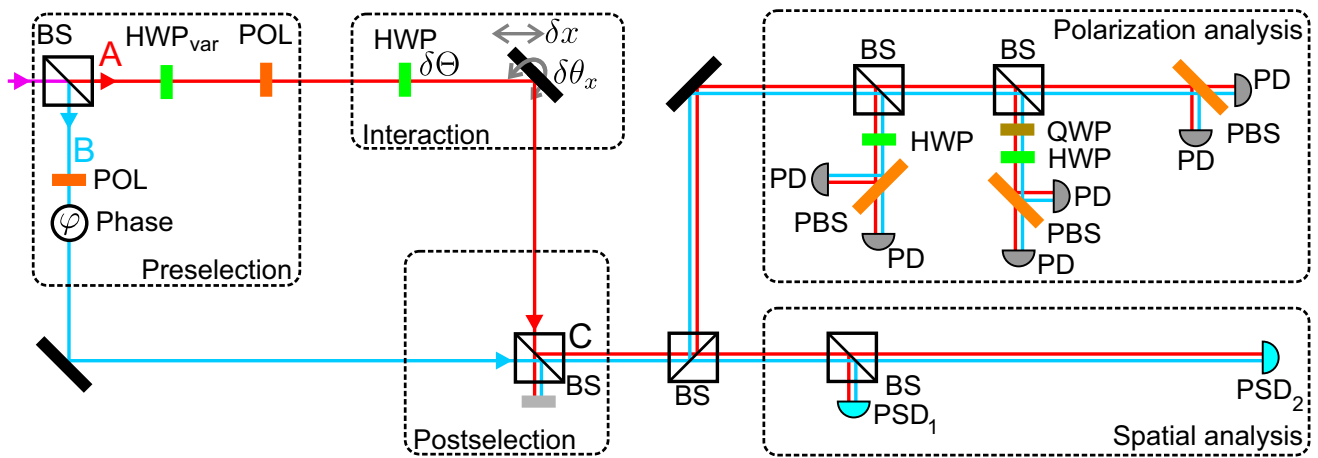


Fig. 3. Schematic experimental setup. The preselection state $|\psi\rangle$ is set by using a nonpolarizing beam splitter (BS), creating a spatial superposition between arms A and B. Two equally oriented polarizers (POL) and a half-wave plate (HWP_{var}) are used to define the relative amplitudes. Angle and position shifts—e.g., $\delta\theta_x$ and δx —are introduced by moving and tilting of optical components, whereas polarization rotations are imposed using a half-wave plate (HWP). The postselection is done by considering only one of the output ports (C) of the interferometer. Analysis of the polarization degree of freedom is achieved by means of half- and quarter-wave plates (QWP), polarizing beam splitters (PBS), and photodiodes (PD), allowing the projection onto the polarization states $1/\sqrt{2}(|H\rangle \pm |V\rangle)$, $1/\sqrt{2}(|H\rangle \pm i|V\rangle)$, $|H\rangle$, and $|V\rangle$. Position-sensing detectors (PSD) at different z-positions allow us to determine position and angle, respectively, in x and in y direction.

a nonpolarizing beam splitter. The moduli of the amplitudes of the preselection state [2] are controlled by means of rotating the polarization using a half-wave plate in arm A, followed by a horizontal polarization filter. The relative phase between the arms φ is set by an optical trombone system with retroreflecting prisms moved by a piezoelectric crystal (not shown).

This setup enables us to directly implement the three desired interactions along beam A and simultaneously measure their effect. Fig. 3 depicts the setup. The spatial displacement δx , which is schematically depicted as a shift of the mirror, was achieved by lateral movement of the prism from the trombone system. Instead of a vertical tilt of this mirror, we incorporate the vertical rotation $\delta\theta_x$ by tilting the second beam splitter. The polarization rotation $\delta\Theta$ is controlled by rotating a half-wave plate in arm A. Detecting light only from the output port C provides the post-selection onto state $|\phi\rangle$, Eq. 4.

The photons at port C are distributed onto several detectors using beam splitters for position and polarization analysis. A position-sensing detector PSD_1 placed near the interferometer and a detector PSD_2 placed farther away allows the estimation of position and angle in x and y directions. We perform tomography of the polarization state using half- and quarter-wave plates in combination with polarizing beam splitters, as shown in Fig. 3.

A measurement run consists of three steps—namely, first a measurement of light propagating in arm A alone, second of arm B alone, and last a measurement of the interference signal. The six expectation values obtained from measurements of arm B are used as a reference for the subsequent analysis.

The measurement with only beam A shows the effect of the interactions when the photons pass through a single channel, as in Fig. 1A. The results are indicated in the graphs of Fig. 4 as red dashed horizontal lines since they exhibit no dependence on the phase.[§]

The universality is clearly shown by the similarity of the results for the three couplings (Fig. 4). Of course, in all graphs, the observed values are different and have different units. For demonstration purposes, we arranged the scales of the graphs

in Fig. 4, *Upper* such that the signals of all interactions, $\langle x \rangle_A$, $\langle \theta_y \rangle_A$, and $\langle \Theta \rangle_A$, have the same size. We were trying to avoid shifts in conjugate variables as much as possible. Our measurement results, red dashed lines in the plots from the Fig. 4, *Lower*, show that the tuning was good, although not perfect.

Continuous violet lines on these graphs provide theoretical predictions based on the weak value $(\mathbf{P}_A)_w$ given by [12], and the interactions in the single arms are presented as red and blue dashed lines in the graphs. The intensities obtained by measuring arm A and arm B alone yield $\tan \alpha = 1.3323 \pm 0.0002$. From the visibility measurement, $\mathcal{V} = 95.09 \pm 0.02\%$, we obtained $\eta = 0.9904 \pm 0.0003$. For these parameters, we observed amplifications with factors up to 4 and -3 . The very good agreement between experimental data and theoretical predictions, shown in Fig. 4, demonstrates the universality of the modification of several fundamentally distinct forms of interactions for couplings with a preselected and postselected system.

To evaluate the dependence of the weak value on the coherence between the two arms parametrized by η , we measured the effect of the displacement in x on the output beam. For this run, we kept the phase fixed at $\varphi = \pi$ and varied the amplitude ratio $\tan \alpha$ covering another region of the parameter space from Fig. 2. We changed the coherence by varying the polarization misalignment, leading to a smaller overlap between the photon states passing through the two arms. The modification of the shift in the x direction presented in Fig. 5 follows nicely the weak value [12].

Alignment Method

In the previous sections, we considered a scenario in which the path state of a photon in an arm of an interferometer is coupled to its other degrees of freedom, in particular, its spatial degrees of freedom in the x and y direction. This scenario exactly represents a situation encountered in real experimental interferometric setups—namely, when the arms of the interferometer are misaligned. The differences in position $\delta\vec{r} \equiv (\delta x, \delta y)$ and angle $\delta\vec{\theta} \equiv (\delta\theta_x, \delta\theta_y)$ between the photons passing through distinct arms of the interferometer can be considered as results of interactions in one arm, which change the initially identical spatial states of the particle.

[§]Please contact J.D. if you desire access to the raw experimental data for this plot as well as for all other plots.

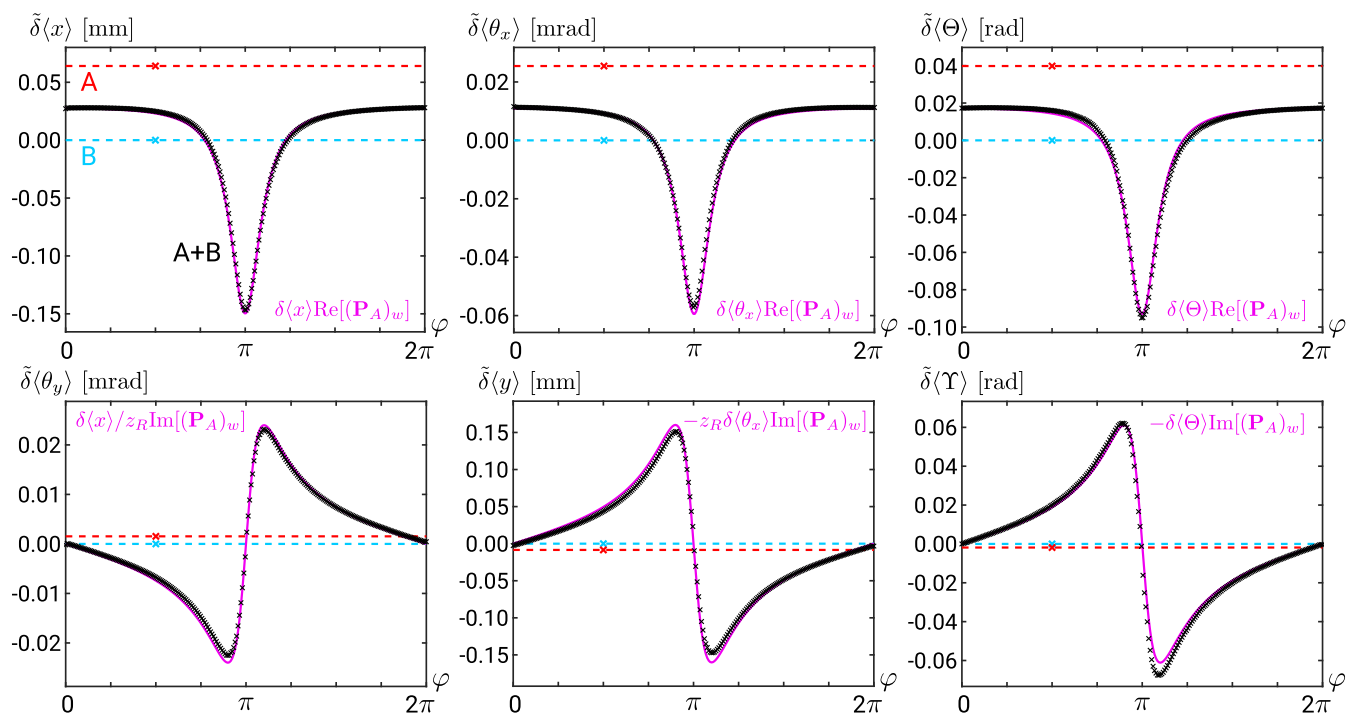


Fig. 4. Observed universality. (Upper) The introduced displacements of arm A in x direction, angle around the x axis, and angle of polarization Θ (δx , $\delta\theta_x$, and $\delta\Theta$) can be seen from the single red datapoints plotted at an arbitrary phase position. The blue datapoints corresponding to arm B are taken as a reference and thus show zero shift. The axes are scaled such that the readings of A agree for the three external systems. For each of these three, the same behavior of the interference signal (black datapoints) is observed for the shifts of the variables $\tilde{\delta}\langle x \rangle$, $\tilde{\delta}\langle \theta_x \rangle$, and $\tilde{\delta}\langle \Theta \rangle$: The effect seen from the measurement of the single arm is multiplied with the phase-dependent real part of the weak value. (Lower) The analogous plots for the shift of the respective conjugate variables represented by $\tilde{\delta}\langle \theta_y \rangle$, $\tilde{\delta}\langle y \rangle$, and $\tilde{\delta}\langle \Upsilon \rangle$ show nicely the dependence on the imaginary part of the weak value. The violet theoretical curves represent the rescaled real and imaginary parts of the weak value (no fit).

It is well known that the picture generated by the interference of the beams from a misaligned interferometer displays a strong phase dependence. Fig. 6A shows the centroid trajectory during

the phase scan of a misaligned interferometer. We demonstrate that it is possible to quantitatively determine the exact misalignment parameters of the interferometer by analyzing this

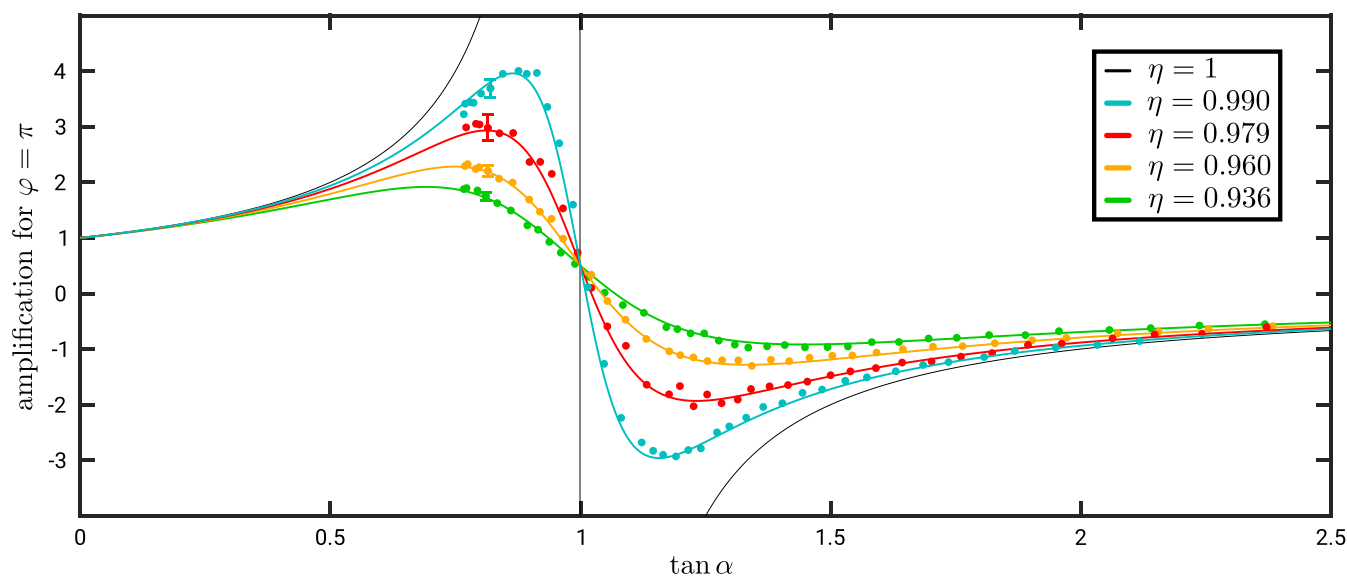


Fig. 5. Modification of weak value due to decoherence. The colored dots represent the measured values for the modification of the shift δx in the interference signal when varying the weak value via the relative amplitudes of the paths A and B ($\tan \alpha$ in Eq. 12) and fixed $\varphi = \pi$. The four datasets correspond to four different values of the overlap η , which quantifies the coherence between the states of the external systems from the two arms. The lines are theoretical curves as highlighted by the colored lines in Fig. 2 C and E. Respective average error bars are shown for each η on one of the first data points. For comparison, also the theoretical line with $\eta = 1$ (Fig. 2A) is shown.

12. Xu X-Y, et al. (2013) Phase estimation with weak measurement using a white light source. *Phys Rev Lett* 111:033604.
13. Dressel J, Malik M, Miatto FM, Jordan AN, Boyd RW (2014) *Colloquium: Understanding quantum weak values: Basics and applications*. *Rev Mod Phys* 86:307–316.
14. Jordan AN, Martínez-Rincón J, Howell JC (2014) Technical advantages for weak-value amplification: When less is more. *Phys Rev X* 4:011031.
15. Ferrie C, Combes J (2014) Weak value amplification is suboptimal for estimation and detection. *Phys Rev Lett* 112:040406.
16. Knee GC, Gauger EM (2014) When amplification with weak values fails to suppress technical noise. *Phys Rev X* 4:011032.
17. Magaña Loaiza OS, Mirhosseini M, Rodenburg B, Boyd RW (2014) Amplification of angular rotations using weak measurements. *Phys Rev Lett* 112:200401.
18. Pusey MF (2014) Anomalous weak values are proofs of contextuality. *Phys Rev Lett* 113:200401.
19. Zhang L, Datta A, Walmsley IA (2015) Precision metrology using weak measurements. *Phys Rev Lett* 114:210801.
20. Piacentini F, et al. (2018) Investigating the effects of the interaction intensity in a weak measurement. *Sci Rep* 8:6959.
21. Martínez-Rincón J, Chen Z, Howell JC (2017) Practical advantages of almost-balanced-weak-value metrological techniques. *Phys Rev A* 95:063804.
22. Li F, Huang J, Zeng G (2017) Adaptive weak-value amplification with adjustable postselection. *Phys Rev A* 96:032112.
23. Araújo MP, De Leo S, Maia GG (2017) Optimizing weak measurements to detect angular deviations. *Annalen der Physik* 529:1600357.
24. Qiu X, et al. (2017) Precision phase estimation based on weak-value amplification. *Appl Phys Lett* 110:071105.
25. Liu X, et al. (2017) Optimal pre- and post-selections of weak measurements for precision parameter estimation. *J Appl Phys* 121:203106.
26. Chen G, et al. (2018) Heisenberg-scaling measurement of the single-photon Kerr nonlinearity using mixed states. *Nat Commun* 9:93.
27. Kim Y, et al. (2018) Direct quantum process tomography via measuring sequential weak values of incompatible observables. *Nat Commun* 9:192.
28. Zhou X, Sheng L, Ling X (2018) Photonic spin hall effect enabled refractive index sensor using weak measurements. *Sci Rep* 8:1221.
29. Li L, et al. (2018) Phase amplification in optical interferometry with weak measurement. *Phys Rev A* 97:033851.
30. Qin L, Wang Z, Zhang C, Li X-Q (2018) Direct measurement of the quantum state of photons in a cavity. *Opt Express* 26:7034–7042.
31. Ren C, Qiu J, Chen J, Shi H (2018) Ultra-precise time tuning and central frequency shift of optical pulses via small weak values. *Opt Commun* 425:19–23.
32. Huang J-Z, Fang C, Zeng G (2018) Weak-value-amplification metrology without spectral analysis. *Phys Rev A* 97:063853.
33. Fang C, Huang J-Z, Zeng G (2018) Robust interferometry against imperfections based on weak value amplification. *Phys Rev A* 97:063818.
34. Li H, et al. (2018) High-precision temperature measurement based on weak measurement using nematic liquid crystals. *Appl Phys Lett* 112:231901.
35. Wu S, Li Y (2011) Weak measurements beyond the Aharonov-Albert-Vaidman formalism. *Phys Rev A* 83:052106.
36. Di Lorenzo A (2012) Full counting statistics of weak-value measurement. *Phys Rev A* 85:032106.
37. Kofman AG, Ashhab S, Nori F (2012) Nonperturbative theory of weak pre- and post-selected measurements. *Phys Rep* 520:43–133.
38. Zhang Y-X, Wu S, Chen Z-B (2016) Coupling-deformed pointer observables and weak values. *Phys Rev A* 93:032128.
39. Denkmayr T, et al. (2017) Experimental demonstration of direct path state characterization by strongly measuring weak values in a matter-wave interferometer. *Phys Rev Lett* 118:010402.
40. Vaidman L (2017) Comment on “Experimental demonstration of direct path state characterization by strongly measuring weak values in a matter-wave interferometer”. arXiv:1703.01616.
41. Aharonov Y, Vaidman L (1990) Properties of a quantum system during the time interval between two measurements. *Phys Rev A* 41:11–20.
42. Wiseman HM (2002) Weak values, quantum trajectories, and the cavity-QED experiment on wave-particle correlation. *Phys Rev A* 65:032111.
43. Silva R, et al. (2014) Pre- and postselected quantum states: Density matrices, tomography, and Kraus operators. *Phys Rev A* 89:012121.
44. Dressel J, Jordan AN (2012) Weak values are universal in Von Neumann measurements. *Phys Rev Lett* 109:230402.
45. Simon C, Polzik ES (2011) Fock-state view of weak-value measurements and implementation with photons and atomic ensembles. *Phys Rev A* 83:040101.
46. Feizpour A, Xing X, Steinberg AM (2011) Amplifying single-photon nonlinearity using weak measurements. *Phys Rev Lett* 107:133603.
47. Fu L, Hashmi FA, Jun-Xiang Z, Shi-Yao Z (2015) An ideal experiment to determine the “past of a particle” in the nested Mach-Zehnder interferometer. *Chin Phys Lett* 32:050303.
48. Ben-Israel A, et al. (2017) An improved experiment to determine the ‘past of a particle’ in the nested Mach-Zehnder interferometer. *Chin Phys Lett* 34:020301.
49. Hallaji M, Feizpour A, Dmochowski G, Sinclair J, Steinberg AM (2017) Weak-value amplification of the nonlinear effect of a single photon. *Nat Phys* 13:540–544.
50. Danan A, Farfurnik D, Bar-Ad S, Vaidman L (2013) Asking photons where they have been. *Phys Rev Lett* 111:240402.
51. Farfurnik D (2013) Weak value analysis of an optical Mach-Zehnder interferometer. Master’s thesis (School of Physics and Astronomy, Tel Aviv University, Tel Aviv).
52. Benschalom N (2017) Quantum weak values in classical interferometry. Master’s thesis (School of Physics and Astronomy, Tel Aviv University, Tel Aviv).
53. Vaidman L (2013) Past of a quantum particle. *Phys Rev A* 87:052104.